9450 *Inorg. Chem.* **2010**, *49*, 9450–9459
DOI: 10.1021/ic101138u

Inorganic Chemistry
Article

Spectroscopic and Computational Studies of an End-on Bound Superoxo-Cu(II) Complex: Geometric and Electronic Factors That Determine the Ground State

Julia S. Woertink,[†] Li Tian,[†] Debabrata Maiti,[‡] Heather R. Lucas,[‡] Richard A. Himes,[‡] Kenneth D. Karlin,[‡,§] Frank Neese,[‖] Christian Würtele,[⊥] Max C. Holthausen,[⊗] Eckhard Bill,[○] Jörg Sundermeyer,[#] Siegfried Schindler,[⊥] and Edward I. Solomon*,[†]

[†] *Department of Chemistry, Stanford University, Stanford, California 94305,* [‡] *Department of Chemistry, Johns Hopkins University, Baltimore, Maryland 21218,* [§] *Department of Bioinspired Science, Ewha Womans University, Seoul 120-750, Korea,* [‖] *Department of Chemistry, University of Bonn, D-53115 Bonn, Germany,* [⊥] *Institut für Anorganische und Analytische Chemie, Justus-Liebig-Universität Giessen, Heinrich-Buff-Ring 58, 35392 Giessen, Germany,* [⊗] *Institut für Anorganische und Analytische Chemie der Johann Wolfgang Goethe-Universität Frankfurt, D-60438 Frankfurt/Main, Germany,* [○] *MPI für Bioanorganische Chemie, 45470 Mülheim an der Ruhr, Germany, and* [#] *Fachbereich Chemie, Philipps-Universität Marburg, Hans-Meerwein-Strasse, D-35032 Marburg, Germany*

Received June 6, 2010

A variety of techniques including absorption, magnetic circular dichroism (MCD), variable-temperature, variable-field MCD (VTVH-MCD), and resonance Raman (rR) spectroscopies are combined with density functional theory (DFT) calculations to elucidate the electronic structure of the end-on (η^1) bound superoxo-Cu(II) complex $[\mathrm{TMG_3trenCuO_2}]^+$ (where $\mathrm{TMG_3tren}$ is 1,1,1-tris[2-[N^2-(1,1,3,3-tetramethylguanidino)]ethyl]amine). The spectral features of $[\mathrm{TMG_3trenCuO_2}]^+$ are assigned, including the first definitive assignment of a superoxo intraligand transition in a metal-superoxo complex, and a detailed description of end-on superoxo-Cu(II) bonding is developed. The lack of overlap between the two magnetic orbitals of $[\mathrm{TMG_3trenCuO_2}]^+$ eliminates antiferromagnetic coupling between the copper(II) and the superoxide, while the significant superoxo π^*_σ character of the copper dz^2 orbital leads to its ferromagnetically coupled, triplet, ground state.

1. Introduction

Copper enzymes perform a number of vital biological functions including O_2 activation and reduction.[1] Enzymes activate O_2 at mononuclear, binuclear, or trinuclear copper sites and catalyze a wide range of reactions.[2] The binuclear copper sites are subdivided into two groups, coupled and noncoupled. The coupled binuclear enzymes include tyrosinase and catechol oxidase, as well as reversible dioxygen binding protein hemocyanin; these proteins activate O_2 using both copper sites to generate peroxy bridged bicupric, Cu_2O_2, sites with strong magnetic interactions (coupling) between the two cupric ions associated with the bridging peroxide.[3] In contrast, the two active site coppers in the noncoupled binuclear enzymes, which include peptidylglycine α-hydroxylating monooxygenase (PHM) and dopamine β-monooxygenase (DβM), are separated by an 11 Å solvent-filled cleft and have no magnetic interaction (i.e., noncoupled).[4] PHM and DβM catalyze the stereospecific hydroxylation of substrate C−H bonds and are involved in neuropeptide and neurotransmitter biosynthesis. PHM catalyzes the hydroxylation of the glycine α-carbon of glycine-extended peptides and DβM catalyzes the conversion of dopamine to norepinephrine.[4] These enzymes activate O_2 at a single copper center (Cu_M in Figure 1A where the "M" refers to the methionine ligand) to generate a reactive mononuclear Cu_M/O_2 intermediate that abstracts a hydrogen atom from the substrate.[5,6] To complete the reaction, an electron is transferred to Cu_M from the second, distant copper site (Cu_H, which has three histidine ligands).[7]

---

*To whom correspondence should be addressed. E-mail: edward.solomon@stanford.edu.

[1] Holm, R. H.; Kennepohl, P.; Solomon, E. I. *Chem. Rev.* **1996**, *96*, 2239–2314.

[2] Solomon, E. I.; Chen, P.; Metz, M.; Lee, S.-K.; Palmer, A. E. *Angew. Chem., Int. Ed.* **2001**, *40*, 4570–4590.

[3] Solomon, E. I.; Tuczek, F.; Root, D. E.; Brown, C. A. *Chem. Rev.* **1994**, *94*, 827–856.

[4] Klinman, J. P. *Chem. Rev.* **1996**, *96*(7), 2541–2562.

[5] Francisco, W. A.; Blackburn, N. J.; Klinman, J. P. *Biochemistry* **2003**, *42*, 1813–1819.

[6] Klinman, J. P. *J. Biol. Chem.* **2006**, *281*(6), 3013–3016.

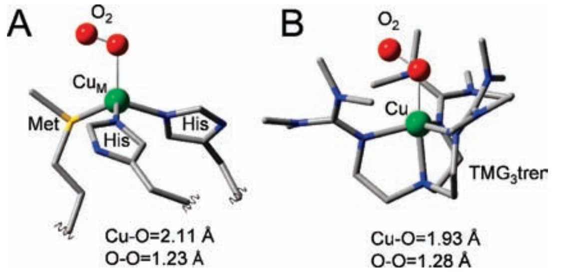

Figure 1. Crystal structures of the precatalytic PHM-O_2 complex[8] (A) and of $[TMG_3trenCuO_2]^{+}$[9] (B).

The identity of the reactive mononuclear Cu_M/O_2 species in PHM and DβM has been the subject of much debate and Cu_M(II)-(hydro)peroxo,[10] Cu_M(II)-superoxo,[11−15] and Cu_M(II)-oxyl[16,17] intermediates have been proposed. Kinetic assays and spectroscopically calibrated density functional theory (DFT) studies have suggested that the key reactive intermediate is a Cu_M(II)-superoxo species formed by the one electron reduction of dioxygen to superoxide ($O_2^{-\bullet}$) by Cu_M(I).[12,13,18,19] The DFT studies were supported by past electronic structure studies on the first crystallographically characterized Cu(II)-superoxo model complex: HB(3-R-5-^{i}Prpz)$_3$CuO$_2$ (where HB(3-R-5-^{i}Prpz)$_3$ = hydrotris(3-*tert*-butyl-5-isopropyl-1-pyrazolyl)- borate).[20] This complex has a side-on (η^2) superoxo-Cu(II) binding mode and a singlet ground state. While both Cu(II) and superoxide independently have $S = 1/2$, the singlet ground state of HB(3-R-5-^{i}Prpz)$_3$CuO$_2$ is not the result of antiferromagnetic coupling between these unpaired electrons. Instead it is the result of the highly covalent copper-superoxo bonding in this complex.[20] A side-on bound-superoxo Cu(II) was computationally evaluated as a possible reactive intermediate in PHM and was shown to be activated for H-atom abstraction.[13]

A recent crystal structure of a precatalytic complex of PHM bound by a slow substrate showed O_2 bound to Cu_M in an end-on (η^1) binding geometry, putatively an end-on bound superoxo-Cu(II) intermediate (Figure 1A).[8] Such end-on bound superoxo-Cu(II) complexes are generally only observed as transient intermediates in the formation of binuclear copper trans-peroxo complexes. However five end-on bound mononuclear superoxo-Cu(II) model complexes have been stabilized and characterized by resonance Raman (rR) spectroscopy.[21−25] One has been crystallographically characterized: $[TMG_3trenCuO_2]^+$ (where TMG$_3$tren is 1,1,1-tris[2-[N^2-(1,1,3,3-tetramethylguanidino)] ethyl]amine) (Figure 1B).[9] From previously published NMR studies, $[TMG_3trenCuO_2]^+$ is paramagnetic, in contrast to the diamagnetic side-on superoxo-Cu(II) complex HB(3-R-5-^{i}Prpz)$_3$CuO$_2$.[26] To understand the nature of end-on superoxide bonding to copper and its relation to the side-on binding mode (described previously as a covalent singlet), detailed experimental and computational studies were performed on $[TMG_3trenCuO_2]^+$. This study also lays the foundation for further studies on whether such a site would be activated toward H-atom abstraction.

In this study absorption, magnetic circular dichroism (MCD), variable-temperature, variable-field (VTVH) MCD, and rR spectroscopies combined with DFT calculations are used to define the electronic structure of $[TMG_3trenCuO_2]^+$. The observed spectral features are assigned; a detailed description of end-on superoxo-Cu(II) bonding and the origin of the paramagnetism of $[TMG_3trenCuO_2]^+$ is developed.

2. Experimental Section

2.1. Preparation of $[TMG_3trenCuO_2]^+$ Samples. [(TMG$_3$-tren)Cu(I)]BArF′ was synthesized using previously published procedures.[27] In an inert atmosphere box, [(TMG$_3$-tren)Cu(I)]BArF′ solution was added to a 25 mL Schlenk flask (2 mM [(TMG$_3$-tren)Cu(I)]BArF′ in either 2MeTHF or THF) and brought out to the benchtop. A 500 μL portion of this solution was taken by syringe and transferred into a Wilmad NMR tube (WG-5M-ECONOMY) equipped with rubber septa, and the solution was cooled to −80 °C. Dioxygen (or $^{18}O_2$: ICON, IO-6393 or $^{16-18}O_2$: ICON, IO-6392) was injected and bubbled via a long needle Hamilton gastight syringe (5 mL), and excess O_2 was removed by vacuum/argon. The resulting solution was frozen in liquid N_2. MCD and low-temperature absorption samples were prepared in a similar manner, and −80 °C [(TMG$_3$-tren)Cu(II)-($O_2^{\cdot -}$)]BArF′ solution (2 mM in 2MeTHF) samples were injected into precooled MCD cells via syringe which were then frozen in liquid N_2 and used for both MCD and low-temperature absorption spectroscopic studies.

2.2. Resonance Raman Spectroscopy. Resonance Raman spectra were obtained using a back-illuminated CCD detector (Princeton Instruments ST-135) on a triple monochromator (Spex 1877 CP with 1200, 1800, and 2400 grooves/mm holographic spectrograph gratings). Excitation was provided by Kr$^+$ (Coherent I90C−K) ion, Ar$^+$ (Innova Sabre 25/7) ion, Dye (Coherent 599 equipped with Rhodamine 6G), and Ti-Sapphire (Coherent 890) lasers with incident power in the 5−100 mW range using an ~135° backscattering configuration. Sample concentration was 2 mM in Cu and spectra were collected on

---

(7) Bell, J.; Meskini, R. E.; D'Amato, D.; Mains, R. E.; Eipper, B. A. *Biochemistry* **2003**, *42*, 7133–7142.

(8) Prigge, S. T.; Eipper, B. A.; Mains, R. E.; Amzel, L. M. *Science* **2004**, *304*(5672), 864–867.

(9) Würtele, C.; Gaoutchenova, E.; Harms, K.; Holthausen, M. C.; Sundermeyer, J.; Schindler, S. *Angew. Chem., Int. Ed.* **2006**, *45*(23), 3867–3869.

(10) Tian, G.; Berry, J. A.; Klinman, J. P. *Biochemistry* **1994**, *33*, 226–234.

(11) Gherman, B. F.; Tolman, W. B.; Cramer, C. J. *J. Comput. Chem.* **2006**, *27*(16), 1950–1961.

(12) Evans, J. P.; Ahn, K.; Klinman, J. P. *Biol. Chem.* **2003**, *278*(50), 49691–49698.

(13) Chen, P.; Solomon, E. I. *J. Am. Chem. Soc.* **2004**, *126*(15), 4991–5000.

(14) de la Lande, A.; Parisel, O.; Gerard, H.; Moliner, V.; Reinaud, O. *Chem.—Eur. J.* **2008**, *14*(21), 6465–6473.

(15) de la Lande, A.; Gerard, H.; Moliner, V.; Izzet, G.; Reinaud, O.; Parisel, O. *J. Biol. Inorg. Chem.* **2006**, *11*(5), 593–608.

(16) Kamachi, T.; Kihara, N.; Shiota, Y.; Yoshizawa, K. *Inorg. Chem.* **2005**, *44*(12), 4226–4236.

(17) Crespo, A.; Marti, M. A.; Roitberg, A. E.; Amzel, L. M.; Estrin, D. A. *J. Am. Chem. Soc.* **2006**, *128*(39), 12817–12828.

(18) Bauman, A. T.; Yukl, E. T.; Alkevich, K.; McCormack, A. L.; Blackburn, N. J. *J. Biol. Chem.* **2006**, *281*(7), 4190–4198.

(19) Chen, P.; Solomon, E. I. *Proc. Natl. Acad. Sci. U.S.A.* **2004**, *101*(36), 13105–13110.

(20) Chen, P.; Root, D. E.; Campochiaro, C.; Fujisawa, K.; Solomon, E. I. *J. Am. Chem. Soc.* **2003**, *125*, 466–474.

(21) Weitzer, M.; Schindler, S.; Brehm, G.; Schneider, S.; Hormann, E.; Jung, B.; Kaderli, S.; Zuberbuhler, A. D. *Inorg. Chem.* **2003**, *42*(6), 1800–1806.

(22) Komiyama, K.; Furutachi, H.; Nagatomo, S.; Hashimoto, A.; Hayashi, H.; Fujinami, S.; Suzuki, M.; Kitagawa, T. *Bull. Chem. Soc. Jpn.* **2004**, *77*(1), 59–72.

(23) Schatz, M.; Raab, V.; Foxon, S. P.; Brehm, G.; Schneider, S.; Reiher, M.; Holthausen, M. C.; Sundermeyer, J.; Schindler, S. *Angew. Chem., Int. Ed.* **2004**, *43*(33), 4360–4363.

(24) Maiti, D.; Fry, H. C.; Woertink, J. S.; Vance, M. A.; Solomon, E. I.; Karlin, K. D. *J. Am. Chem. Soc.* **2007**, *129*(2), 264–265.

(25) Kunishita, A.; Kubo, M.; Sugimoto, H.; Ogura, T.; Sato, K.; Takui, T.; Itoh, S. *J. Am. Chem. Soc.* **2009**, *131*(8), 2788–2789.

(26) Lanci, M. P.; Smirnov, V. V.; Cramer, C. J.; Gauchenova, E. V.; Sundermeyer, J.; Roth, J. P. *J. Am. Chem. Soc.* **2007**, *129*(47), 14697–14709.

(27) Raab, V.; Kipke, J.; Burghaus, O.; Sundermeyer, J. *Inorg. Chem.* **2001**, *40*(27), 6964–6971.

frozen tetrahydrofuran (THF) solutions or 2MeTHF frozen glasses in NMR tubes cooled to 77 K in a liquid nitrogen finger Dewar (Wilmad). Background spectra of charcoal in NMR tubes were used for baseline subtraction. Peak intensities were determined relative to solvent bands. A normal coordinate analysis (NCA) was performed using the program VIBRATZ (version 2.2, Shape Software).[28,29]

2.3. Low-Temperature Absorption Spectroscopy. Low-temperature absorption spectra were obtained using a Cary 500 double-beam spectrophotometer (Varian) with a liquid helium cryostat (Janis Research Super Vari-Temp). Low-temperature absorption and MCD spectra were simultaneously fit using the program PeakFit (Version 4.06, AISN Software).

2.4. Magnetic Circular Dichroism. MCD spectra were collected on CD spectropolarimeters with modified sample compartments to accommodate magnetocryostats. UV−vis data were collected on a Jasco J810−150S spectrometer with either a S1 or a S20 photomultiplier tube (Hamamatsu) and equipped with an Oxford Instruments SM4000−8T magnet. Near-IR spectra were collected on a Jasco J200 equipped with a liquid N_2-cooled InSb detector and equipped with an Oxford Instruments SM4000-7 T magnet. MCD spectra were measured at fields from 0 to ±7 T and temperatures from 1.78 to 100 K. VTVH MCD data were collected using a calibrated Cernox resistor (Lakeshore Cryogenics, calibrated 1.5−300 K) inserted into the sample cell to accurately measure the sample temperature. VTVH MCD data were normalized for each wavelength to the maximum observed intensity over all isotherms.

2.5. Electronic Structure Calculations. Spin unrestricted DFT calculations were performed with Gaussian 03.[30] The geometry of $[\mathrm{TMG_3trenCuO_2}]^+$ was fully optimized starting from the X-ray crystal structure coordinates. Calculations were performed with the B3LYP functional[31] and with the BP38 (38% Hartree−Fock exchange added to the BP86 functional), and BP86 functionals.[32,33] Geometry optimization, frequency calculations, and TD-DFT calculations were performed using the 6-311G* basis set.[34] Single point energy calculations were performed on optimized geometries using the 6-311+G* basis set. Tight convergence criteria (10^{-8} E_H in energy) were used for all calculations. Wave functions were visualized and orbital contour plots were generated using GaussView,[35] and population analyses were performed with QMForge.[36] TD-DFT results were plotted with SWizard.[37]

3. Results and Analysis

3.1. Absorption and MCD. Low temperature absorption and MCD spectra of a frozen glass of $[\mathrm{TMG_3trenCuO_2}]^+$ (5 K, 2MeTHF) are shown in Figure 2 and are simultaneously fit with five Gaussian-resolved bands. The transition energies, extinction coefficients, and C_0/D_0 ratios for these bands are given in Table 1. The most intense absorption feature of $[\mathrm{TMG_3trenCuO_2}]^+$ is at 22,500 cm^{-1} (ε = 3,500 M^{-1} cm^{-1}) (Figure 2A, Band 5). Four less intense absorption features are observed at 14,800 cm^{-1} (Band 4, ε = 1,475 M^{-1} cm^{-1}), 13,000 cm^{-1} (Band 3, ε = 450 M^{-1} cm^{-1}), 11,670 cm^{-1} (Band 2, ε = 815 M^{-1} cm^{-1}) and 10,100 cm^{-1} (Band 1, ε = 290 M^{-1} cm^{-1}) (Figure 2A). Band 3 is required to account for the intensity between Bands 2 and 4 in the absorption spectrum, but it is not necessary to accurately fit the MCD spectrum, indicating that Band 3 has very low MCD intensity. Justification for the presence of Band 3, as well as its assignment is presented in Sections 3.4 and 3.6.2.

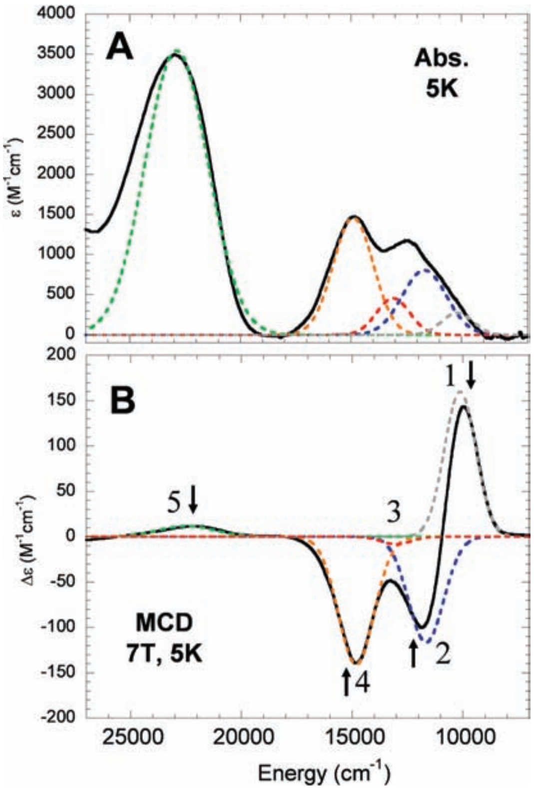

Figure 2. Low temperature absorption (A) and MCD (B) spectra of $[\mathrm{TMG_3trenCuO_2}]^+$. VTVH collection points are marked with arrows (see Section 3.2).

Table 1. Summary of Gaussian-Resolved Absorption and MCD Bands of $[\mathrm{TMG_3trenCuO_2}]^+$

band	energy/cm^{-1}	ε /M^{-1} cm^{-1}	$\Delta\varepsilon$ /M^{-1} cm^{-1}	C_0/D_0
1	10,100	290	159	0.50
2	11,670	815	−117	−0.10
3	13,000	450	−5	−0.007
4	14,820	1475	−139	−0.10
5	22,500	3500	12	0.003

Four intense bands are observed in the MCD spectrum of $[\mathrm{TMG_3trenCuO_2}]^+$ (Figure 2B). Bands 1 and 5 have positive intensity and bands 2 and 4 have negative intensity. The two lowest energy features, Bands 1 and 2, form a derivative shaped pseudo-*A* term. The observed MCD features show field and temperature dependence consistent with C-term behavior (see below and Supporting Information, Figure S1).[38] The presence of intense, C-term MCD features requires that $[\mathrm{TMG_3trenCuO_2}]^+$ is

---

(28) *VIBRATZ,* , V2.2; Shape Software: Kingsport, TN, 2010; http://www.shapesoftware.com/.

(29) Dowty, E. *Phys. Chem. Miner*. **1987**, *14*, 67–79.

(30) Frisch, M. J. et al. *Gaussian 03*, Revision C.02; Gaussian, Inc.: Wallingford, CT, 2003.

(31) Becke, A. D. *J. Chem. Phys.* **1993**, *98*, 5648–5652 (B3LYP).

(32) Becke, A. D. *Phys. Rev. A* **1988**, *38*(6), 3098–3100.

(33) Perdew, J. P. *Phys. Rev. B* **1986**, *33*, 8822–8824.

(34) Rassolov, V.; Pople, J. A.; Ratner, M.; Redfern, P. C.; Curtiss, L. A. *J. Comput. Chem.* **2001**, *22*(9), 976–984.

(35) Dennington, R., II; Keith, T.; Millam, J.; Eppinnett, K.; Hovell, W. L.; Gilliland, R. *GaussView*, Version 3.09; Semichem, Inc.: Shawnee Mission, KS, 2003.

(36) Tenderholt, A. L. *QMForge*, Version 2.1; Stanford University: Stanford, CA, 2007.

(37) Gorelsky, S. I. *SWizard Program*; University of Ottawa: Ottawa, Canada, 2010; http://www.sg-chem.net/.

(38) Piepho, S. B.; Schatz, P. N. *Group Theory in Spectroscopy with Application to Magnetic Circular Dichroism*; John Wiley & Sons, Inc.: New York, 1983.

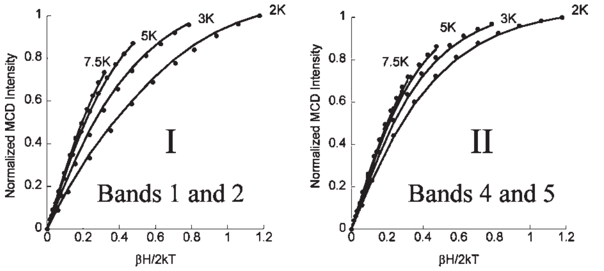

Figure 3. VTVH MCD data of $[TMG_3trenCuO_2]^+$ (dots) with fits (curves).

paramagnetic, consistent with previously published NMR studies.[26]

Bands 1, 2, and 4 have high MCD intensity and relatively low absorption intensity, reflected in the high magnitude of their C_0/D_0 ratios (0.50, −0.10, and −0.10 respectively) (Table 1). In contrast, Band 5 has low MCD intensity and high absorption intensity and thus a relatively low C_0/D_0 magnitude (0.003). MCD C-term intensity is gained through spin−orbit coupling (SOC), and because the SOC interaction is much stronger for copper (ξ[Cu(II)] = 830 cm^{-1}) than for nitrogen or oxygen (ξ[N, O]~60−70 cm^{-1}), copper-centered d→d transitions have significantly larger C_0/D_0 ratios than charge transfer transitions.[39,40] From the C_0/D_0 ratios in Table 1, Bands 1, 2, and 4 are assigned as copper d→d transitions and Band 5 is assigned as a charge transfer transition.

3.2. VTVH-MCD. From the temperature dependent MCD intensity, the ground state of $[TMG_3trenCuO_2]^+$ is paramagnetic; from the variable-temperature, variable-field (VTVH) MCD data presented below (Figure 3) it is determined to have an $S = 1$ ground state.

In VTVH-MCD, saturation magnetization curves are collected at several fixed temperatures with varying magnetic field and are plotted as a function of $\beta H/2kT$. For an $S = 1/2$ complex these isotherms superimpose, but for $S > 1/2$ systems, they spread out because of zero-field splitting (ZFS) and are said to be nested. The VTVH-MCD isotherms collected for $[TMG_3trenCuO_2]^+$ at wavelengths corresponding to each observed MCD feature (Figure 2, arrows) are nested (Figure 3), conclusively ruling out the possibility that the observed paramagnetism in $[TMG_3trenCuO_2]^+$ is from an $S = 1/2$ species (contaminant or decay product) and confirming that the ground state of $[TMG_3trenCuO_2]^+$ is a triplet ($S = 1$).

The VTVH-MCD saturation magnetization behavior in Figure 3 is a reflection of the ground state spin Hamiltonian parameters of $[TMG_3trenCuO_2]^+$ and of the polarizations of the corresponding transitions. A schematic of the ground state triplet ($S = 1$) and excited state singlet ($S = 0$, higher in energy by 2J, where J is the exchange coupling) of $[TMG_3trenCuO_2]^+$, is shown in Figure 4. The $S = 1$ ground state has three M_s sublevels (0, ±1). ZFS breaks the degeneracy of these levels, which can be modeled by axial (D) and rhombic (E) ZFS parameters (Figure 4). The magnitude and sign of D and the ratio of E/D in $[TMG_3trenCuO_2]^+$ are determined from fits of the VTVH-MCD isotherms.

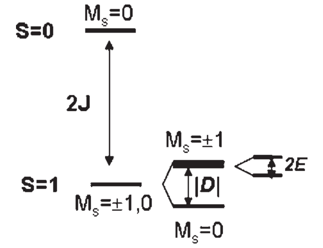

Figure 4. Schematic ground-state energy diagram for $[TMG_3trenCuO_2]^+$.

Two types of saturation behaviors were observed for $[TMG_3trenCuO_2]^+$ (Figure 3); Bands 1 and 2 show the same nesting behavior (Behavior I), distinct from that of Bands 4 and 5 (Behavior II). To analyze the experimental saturation magnetization curves, a Simplex algorithm was used to fit the spin Hamiltonian parameters (eq 1) along with the effective transition moment products ($M_{uv}{}^{\mathrm{eff}}$, eq 2) of the two experimentally observed nesting patterns of $[TMG_3trenCuO_2]^+$ (Figure 3). The $M_{uv}{}^{\mathrm{eff}}$ are the products of the polarizations of the electronic transitions (u, v = x, y, z). As all of the observed MCD features are from the same ground state, this different nesting behavior must result from different transition polarizations. The two nesting patterns were fit to obtain the axial (D) and rhombic (E) ZFS parameters, allowing the $M_{uv}{}^{\mathrm{eff}}$ values to vary for behavior I and II. The polarizations of the transitions, relative to the ZFS axis (the Cu−O bond, defined as the z-axis), were calculated from the resulting $M_{uv}{}^{\mathrm{eff}}$ values by applying and cycling x, y, z in eq 3 (see ref 41 for definitions of the parameters).[41]

$$\hat{H}_{spin} = \beta_{\mathrm{B}}\vec{B}g\vec{S} + D[S_z^2 - (1/3)S(S+1)] + E[S_x^2 - S_y^2] \qquad (1)$$

$$\frac{\Delta\varepsilon}{E} = \frac{\gamma}{4\pi S}\int_0^{\pi}\int_0^{2\pi}\sum_i N_i(l_z\langle S_z\rangle_i M_{xy}^{eff} + l_y\langle S_y\rangle_i M_{xz}^{eff} + l_x\langle S_x\rangle_i M_{yz}^{eff})\sin\theta\, \mathrm{d}\theta\, \mathrm{d}\phi\, r \qquad (2)$$

$$\%x = 100 \times \left[\frac{(M_{xy}^{eff}M_{xz}^{eff})^2}{(M_{xy}^{eff}M_{xz}^{eff})^2 + (M_{xy}^{eff}M_{yz}^{eff})^2 + (M_{yz}^{eff}M_{xz}^{eff})^2}\right] \qquad (3)$$

From this analysis of $[TMG_3trenCuO_2]^+$ $D = +1.2$ cm^{-1}. This positive ZFS establishes that $M_s = 0$ is the ground state (Figure 4). The E/D ratio of the complex is 0.02 signifying that $[TMG_3trenCuO_2]^+$ is highly axial and the $M_s = \pm 1$ sublevels are not significantly split. The fits of the two nesting patterns are included in Figure 3 and accurately reproduce experiment. Both fits reflect the same D (+1.2 cm^{-1}) and E/D (0.02), but have different polarizations

---

(39) Solomon, E. I.; Hanson, M. A. Bioinorganic Spectroscopy. In *Inorganic Electronic Structure and Spectroscopy*; Solomon, E. I., Lever, A. B. P., Eds.; John Wiley & Sons, Inc.: New York, 1999; Vol. *2*, pp 1−130.

(40) Solomon, E. I.; Pavel, E. G.; Loeb, K. E.; Campochiaro, C. *Coord. Chem. Rev.* **1995**, *144*, 369–460.

(41) Neese, F.; Solomon, E. I. *Inorg. Chem.* **1999**, *38*(8), 1847–1865.

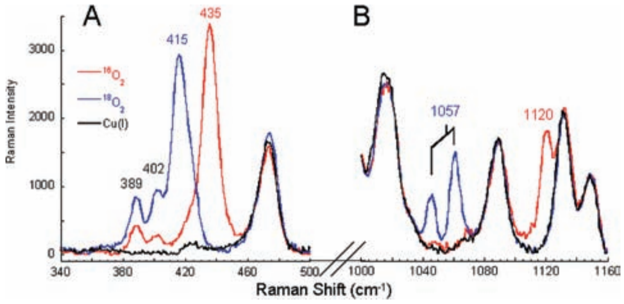

Figure 5. rR spectra of $[\mathrm{TMG_3trenCuO_2}]^+$ with $^{16}O_2$ (red) and $^{18}O_2$ (blue) isotopic substitution in the region of ν(Cu−O) (A) and ν(O−O) (B) (λ_{ex} = 457.9 nm, 20 mW power, 77 K).

relative to the ZFS axis: Bands 1 and 2 (Behavior I) are *x,y* polarized, while Bands 4 and 5 (Behavior II) are *z*-polarized (i.e., along the copper-superoxo bond).

3.3. Resonance Raman. The rR spectrum of a frozen glass of $[\mathrm{TMG_3trenCuO_2}]^+$ (2MeTHF, 77 K) is shown in Figure 5. With excitation within the dominant absorption feature (Band 5, Figure 5A) (λ_{ex} = 457.9 nm), resonantly enhanced bands are observed at 389, 402, 435, and 1120 cm^{-1} (Figure 5, red). Upon $^{18}O_2$-labeling of the complex, two bands shift to lower energy (435 cm^{-1} ($\Delta^{18}O_2 = -20$ cm^{-1}) and 1120 cm^{-1} ($\Delta^{18}O_2 = -63$ cm^{-1})), indicating these modes have significant oxygen character. The 435 cm^{-1} band shifts to 415 cm^{-1} (Figure 5A, blue) and is assigned as the Cu−O stretch (ν(Cu−O)) based on its energy and isotope shift. The energy of the 1120 cm^{-1} band is consistent with the previously published O−O stretch (ν(O−O)) of $[\mathrm{TMG_3trenCuO_2}]^+$ (1117 cm^{-1} in acetone, −70 °C)[23] and of the end-on bound superoxo-Cu(II) complex $[\mathrm{NMe_2TMPACuO_2}]^+$ (1121 cm^{-1} in THF, 77 K).[24] The O−O stretch is observed as a single peak when the complex is formed with $^{16}O_2$ (Figure 5B, red), but is observed as two features when the complex is formed with $^{18}O_2$ (Figure 5B, blue). This behavior is consistent with a Fermi resonance of the $^{18}O_2$-vibration with a non-enhanced mode at similar energy. Using the intensity-weighted average energy of the two observed mixed-modal features, the pre-interaction energy of the resonantly enhanced $\nu(^{18}O-^{18}O)$ is calculated to be 1057 cm^{-1}. Thus, the 1120 cm^{-1} vibration (ν(O−O)) shifts down in energy by 63 cm^{-1} upon $^{18}O_2$-substitution, and its energy is consistent with a superoxo-level species.

The bands at 402 and 389 cm^{-1} (Figure 5A) do not shift upon $^{18}O_2$-isotopic substitution and have energies consistent with Cu−N vibrations. On the basis of their relative energies, the 402 cm^{-1} vibration is assigned as equatorial, guanidinium N−Cu stretch ($\nu(\mathrm{Cu-N_{eq}})$), and the 389 cm^{-1} vibration is assigned as the axial amine N−Cu stretch ($\nu(\mathrm{Cu-N_{ax}})$). $\nu(\mathrm{Cu-N_{ax}})$ is assigned as the lower energy stretch based on the longer $\mathrm{Cu-N_{ax}}$ bond (2.128 Å) relative to average $\mathrm{Cu-N_{eq}}$ (2.092 Å) resolved in the crystal structure of $[\mathrm{TMG_3trenCuO_2}]^+$.[9]

To probe if solvent has an effect on the observed vibrations, rR spectra of $[\mathrm{TMG_3trenCuO_2}]^+$ were also collected in THF at 77 K (Supporting Information, Figure S2). The band energies, relative intensities, and isotopic shifts were identical in both solvent systems.

The crystal structure of $[\mathrm{TMG_3trenCuO_2}]^+$ clearly establishes the end-on binding mode of the superoxo in the solid, crystalline form.[9] To confirm the end-on binding mode of the superoxo to Cu in 2MeTHF, $[\mathrm{TMG_3trenCuO_2}]^+$ was generated with a mixed-isotope gas containing a 1:2:1 stoichiometric mixture of $^{16}O_2/^{16/18}O_2/^{18}O_2$ ($^{16/18}O_2$). In the rR spectrum of $[\mathrm{TMG_3trenCu}(^{16/18}O_2)]^+$, two Cu−O stretches, overlaying the pure isotope stretches, were observed (Supporting Information, Figure S3). The absence of an intermediate Cu−O stretching feature (~425 cm^{-1}) confirms that the superoxo is bound end-on to Cu in 2MeTHF, as it is in the solid, crystalline form.[24,42]

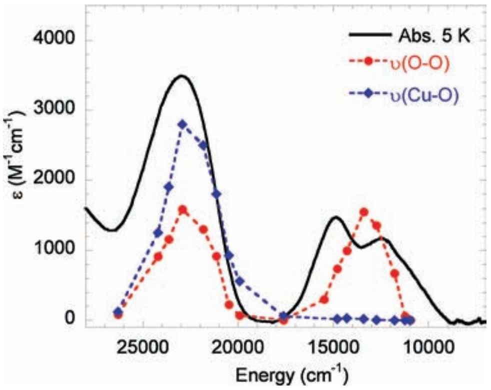

Figure 6. Low temperature (5 K) absorption spectrum of $[\mathrm{TMG_3trenCuO_2}]^+$ (black) and rR profile for ν(Cu−O) (435 cm^{-1}, blue) and ν(O−O) (1120 cm^{-1}, red) (77 K).

A normal coordinate analysis was performed on a triatomic ($\mathrm{CuO_2}$) model with geometric parameters taken from the crystal structure of $[\mathrm{TMG_3trenCuO_2}]^+$. Using the experimentally observed energies for ν(O−O), ν(Cu−O), force constants were obtained for the O−O and Cu−O bonds of the complex. The O−O bond has a force constant of 5.76 mdyn/Å, typical of a superoxide;[43] and the force constant for the Cu−O bond of $[\mathrm{TMG_3trenCuO_2}]^+$ is 1.64 mdyn/Å (see Supporting Information, Table S2 for the force field).

3.4. rR Profiles and Excited State Distortions. The rR excitation profiles for ν(Cu−O) (435 cm^{-1}) and ν(O−O) (1120 cm^{-1}) of $[\mathrm{TMG_3trenCuO_2}]^+$ are shown in Figure 6, overlaid with the low temperature absorption spectrum (Figure 6, black) of the complex. Both ν(Cu−O) (Figure 6, blue) and ν(O−O) (Figure 6, red) are significantly enhanced within the absorption envelope of Band 5, which was assigned as a charge transfer transition based on its low C_0/D_0 ratio (Section 3.1). The enhancement of both ν(Cu−O) and ν(O−O) within Band 5 indicates that the Cu−O and O−O bonds are significantly distorted in the associated excited state; thus, Band 5 is assigned as a superoxo to Cu(II) ligand-to-metal charge-transfer (LMCT) transition. ν(Cu−O) is only enhanced in Band 5 and has no significant enhancement within any of the lower energy absorption bands. ν(O−O) has a different behavior, however, and is significantly enhanced in intensity between Bands 2 and 4, profiling through Band 3 (Figure 2). Thus, Band 3 corresponds to an electronic transition with considerable distortion of the O−O bond

---

(42) Pate, J. E.; Cruse, R. W.; Karlin, K. D.; Solomon, E. I. *J. Am. Chem. Soc.* **1987**, *109*(9), 2624–2630.

(43) Nakamoto, K. *Infrared and Raman Spectra of Inorganic and Coordination Compounds; Part A: Theory and Applications in Inorganic Chemistry*, 5th ed.; John Wiley & Sons, Inc.: New York, 1997.

and little distortion of the Cu−O bond in the excited state. The excited state distortions associated with Band 3 relative to the distortions associated with Band 5, the superoxo to Cu(II) CT allow the definitive assignment of Band 3.

Quantitative excited-state distortions in two modes (n and m) within an excited state can be obtained by relating the ratio of their intensities in preresonance to their energies (ν) and dimensionless excited-state displacement parameters along each normal-coordinate (Δ) by eq 4.[44]

$$\frac{I_n}{I_m} \approx \frac{\Delta_n{}^2 \nu_n{}^2}{\Delta_m{}^2 \nu_m{}^2} \tag{4}$$

As the bandwidth of the observed absorption feature is the result of Franck−Condon progressions along these coordinates, the bandwidth of the low temperature absorption spectrum is related to Δ by eq 5.[45]

$$fwhm \approx [4 \ln 2 \sum_k \Delta_k{}^2 \nu_k{}^2]^{1/2} \tag{5}$$

Applying eq 4 to calculate the ratio of the Cu−O and O−O distortions, $|\Delta_{\mathrm{Cu-O}}|/|\Delta_{\mathrm{O-O}}|$ is found to be 3.38:1 within the superoxo to Cu(II) CT transition (Band 5). From eq 5, $|\Delta_{\mathrm{Cu-O}}| = 3.28$ and $|\Delta_{\mathrm{O-O}}| = 0.97$ in Band 5. Δ_n is related to the excited state relaxation energy ($E_{R(n)}$) for a distortion along mode ν_n by eq 6.[46] The excited state internal coordinate distortion (Δr_i) is obtained from Δ_n using eq 7, where $l_{n,i}$ is the ith element of L_n, the mass-weighted eigenvector for the nth normal mode.

$$E_{R(n)} = \left(\frac{\Delta_n{}^2}{2}\right)\nu_n \tag{6}$$

$$\Delta r_i(\text{Å}) = 5.8065 \sum_n l_{n,i}(\Delta_n/\sqrt{\nu_n}) \tag{7}$$

From eq 6, in the superoxo to Cu(II) CT transition (Band 5), the excited state relaxation energy associated with the displacement along the Cu−O normal mode is 2,360 cm^{-1} and 530 cm^{-1} for the displacement along the O−O normal mode. Further, in this electronic transition, the magnitudes of the excited state distortions of the Cu−O and O−O bonds are 0.26 Å and 0.06 Å, respectively.

In the excited state associated with Band 3, the only significant distortion occurs along the O−O bond, as revealed by the rR profiles for the ν(O−O) and ν(Cu−O) modes and eq 5. From eq 6 the excited-state relaxation energy for the displacement along the O−O in Band 3 is 1430 cm^{-1}. This ratio of the distortion energies in the O−O stretch in Band 5 (530 cm^{-1}) to Band 3 (1430 cm^{-1}) reflects the ratio of the square of the distortions (Δr^2) of the O−O bond in Band 5 to that in Band 3. This gives an excited state distortion of the O−O bond in Band 3 of 0.10 Å. Thus, the O−O is considerably more distorted in Band 3 (0.10 Å) as compared to in Band 5, the superoxo to Cu(II) CT transition (0.06 Å). The results of this analysis are summarized in Table 2.

Table 2. Excited State Distortions of the Cu−O and O−O Bonds

	Band 5 (LMCT)	Band 3
$\lvert\Delta_{\mathrm{O-O}}\rvert$	0.97	1.6
$\lvert\Delta_{\mathrm{Cu-O}}\rvert$	3.28	~0
$E_{\mathrm{O-O}}$	530 cm^{-1}	1,430 cm^{-1}
$E_{\mathrm{Cu-O}}$	2,360 cm^{-1}	~0
$\Delta r_{\mathrm{O-O}}$	0.06 Å	0.10 Å
$\Delta r_{\mathrm{Cu-O}}$	0.26 Å	~0

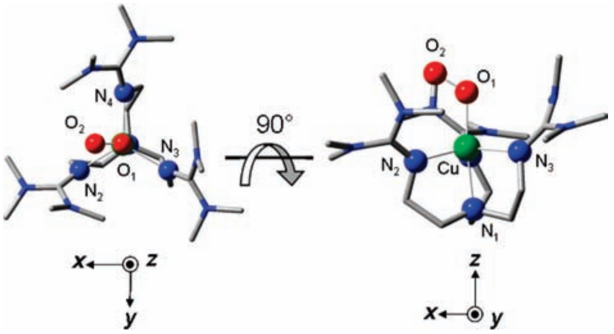

Figure 7. DFT-optimized geometry of [TMG$_3$trenCuO$_2$]$^+$.

Table 3. Experimentally Observed and DFT Calculated Geometry and Vibrational Frequencies of [TMG$_3$trenCuO$_2$]$^+$

geometry /Å			vibrational frequencies (Δ^{18}O$_2$) /cm^{-1}		
	exp.	calc.		exp.	calc.
r(Cu−O$_1$)	1.927	1.954	ν(Cu−O)	435 (−20)	422 (−17)
r(O$_1$−O$_2$)	1.280	1.289	ν(O−O)	1120 (−63)	1213 (−73)
r(Cu−N$_1$)	2.128	2.174	ν(Cu−N$_{\mathrm{ax}}$)	389 (0)	380 (0)
r(Cu−N$_2$)	2.080	2.117	ν(Cu−N$_{\mathrm{eq}}$)	402 (0)	394 (0)
r(Cu−N$_3$)	2.101	2.163			
r(Cu−N$_4$)	2.095	2.148			
∠Cu−O$_1$−O$_2$	123.5°	121.0°			

3.5. DFT Calculations. Spin-unrestricted DFT calculations were performed with Gaussian 03 to gain insight into the bonding interactions and the electronic structure of [TMG$_3$trenCuO$_2$]$^+$.[47] A model of the [TMG$_3$trenCuO$_2$]$^+$ complex was constructed starting from the crystal structure of the complex and fully geometry optimized (Figure 7). The geometric parameters of the model optimized using DFT with the unrestricted B3LYP functional are shown in Table 3 and are in reasonable agreement with the experimentally observed values. The DFT calculations on this model accurately predict the experimentally observed $S = 1$ ground state for the complex; the $S = 0$ state has almost the same optimized geometry as the $S = 1$ ground state and is 7.0 kcal/mol higher in energy.[48] The DFT-calculated frequencies reasonably predict the energies and isotope shifts of the experimentally observed ν(Cu−O), ν(O−O), ν(Cu−N$_{\mathrm{ax}}$), and ν(Cu−N$_{\mathrm{eq}}$) (Table 3).

3.6. Band Assignments and TD-DFT. A schematic energy level diagram of the molecular orbitals (MOs) of the approximately trigonal bipyramidal [TMG$_3$trenCuO$_2$]$^+$

---

(44) Warshel, A. *Annu. Rev. Biophys. Bioeng.* **1977**, *6*, 273–300.

(45) Solomon, E. I. *Comments Inorg. Chem.* **1984**, *3*, 227.

(46) Huang, K. *Proc. R. Soc. A* **1951**, *208*(1094), 352–365.

(47) Three different functionals were evaluated (BP86, B3LYP, and BP38). All three give qualitatively the same results (Supporting Information, Figure S4). The results of the B3LYP calculations are presented in the text.

(48) This energy has been corrected to eliminate triplet-state spin contamination from the broken symmetry singlet excited state using the Yamaguchi formula[50] $^1E = (2^{\mathrm{BS}}E - \langle S^2\rangle_{\mathrm{BS}}{}^3E)/(2 - \langle S^2\rangle_{\mathrm{BS}})$.

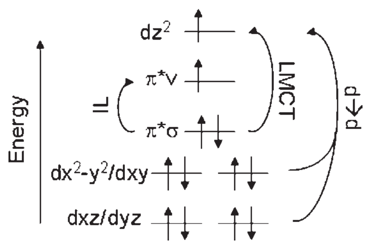

Figure 8. Schematic energy level diagram of $[TMG_3trenCuO_2]^+$ showing possible electronic transitions.

Table 4. TD-DFT Calculated Transition Energies, Oscillator Strengths (f_{osc}), and Polarizations of $[TMG_3trenCuO_2]^+$

transition	assignment	energy (cm^{-1})	f_{osc}	x,y pol. (%)	z-pol. (%)
$\pi^*_\sigma \rightarrow \pi^*_v$	IL	7,199	0.0000	100	0
$dxy \rightarrow dz^2$	d→d	10,443	0.0026	99	1
$dx^2-y^2 \rightarrow dz^2$	d→d	10,545	0.0028	98	2
$dyz \rightarrow dz^2$	d→d	16,248	0.0008	27	73
$dxz \rightarrow dz^2$	d→d	16,679	0.0042	3	97
$\pi^*_\sigma \rightarrow dz^2$	LMCT	17,801	0.0373	5	95
$dxy \rightarrow \pi^*_v$	MLCT	24,450	0.0008	76	24
$dx^2-y^2 \rightarrow \pi^*_v$	MLCT	24,694	0.0031	3	97

in idealized C_{3v} symmetry is shown in Figure 8.[49] π^*_σ refers to the superoxo π^* orbital in the CuO_2 plane and σ-bonding to the Cu(II) dz^2 orbital and π^*_v refers to the superoxo π^* orbital perpendicular to the CuO_2 plane. In this C_{3v} symmetric limit the occupied dx^2-y^2 and dxy orbitals are degenerate, as are the dxz/dyz orbitals and the single hole on the Cu(II) is in the dz^2 orbital. From this diagram, d→d transitions are predicted to the dz^2 orbital from the doubly degenerate dx^2-y^2/dxy and from the doubly degenerate dxz/dyz (Figure 8). The transition from the degenerate dxz/dyz to dz^2 is predicted at higher energy than the transition from the degenerate dx^2-y^2/dxy to dz^2. A superoxo π^*_σ to copper dz^2 charge transfer (LMCT) is also predicted, as is a superoxo $\pi^*_\sigma \rightarrow \pi^*_v$ intraligand transition (IL) (Figure 8). This diagram also allows for the possibility of a metal to ligand charge transfer (MLCT) transition from the occupied copper d to the superoxo π^*_v orbital (MLCT); however, from TD-DFT calculations (vide infra; Table 4), the MLCT transitions will be at higher energy than the LMCT transition (by about 7000 cm^{-1}) and not experimentally observed.

3.6.1. d→d Transitions. From Figure 8, two sets of d→d transitions are predicted for $[TMG_3trenCuO_2]^+$. From the experimentally observed low temperature absorption and MCD spectra of the complex (Figure 2), three bands are observed which are assigned as d→d transitions based on their C_0/D_0 ratios (Bands 1, 2, and 4). Band 1 has positive MCD intensity and forms a pseudo-A term with the negative Band 2. Analysis of their VTVH behaviors revealed Bands 1 and 2 are both x,y-polarized (Section 3.2). Band 4 has negative MCD intensity and is z-polarized. An analysis was performed for the copper-center of $[TMG_3trenCuO_2]^+$ to determine the predicted sign and splitting of the d→d transitions and aid in their assignments. As the d→d transitions are localized on the Cu(II) which couples to the superoxo to give the total $S = 1$ ground state, their properties in the $S = 1$ radical pair (resulting from interaction of the $S = 1/2$ Cu(II) and $S = 1/2$ superoxo) are determined by the ligand field of the Cu(II). This has an orbitally nondegenerate $^2A_1$ ground state. With the introduction of a magnetic field along the molecular z-axis the Zeeman effect splits the $\pm 1/2$ m_s levels, resulting in an $m_s = -1/2$ ground state (Ψ_1). At low temperature only this ground state is populated, and thus the d→d transitions observed in MCD are all from the Ψ_1 initial state in Figure 9. The two ligand field excited states (dxy/dx^2-y^2 and dxz/dyz) are both doubly degenerate ^2E states. The lower energy ^2E, corresponding to excitation of an electron from dxy, dx^2-y^2 to dz^2, splits into two states separated by $|2\lambda|$ (~1660 cm^{-1}) through spin−orbit coupling (SOC). Applying the Zeeman effect (ZE) splits each of these states into two Zeeman states. For a transition to be MCD allowed $\Delta M_S = 0$, thus two transitions in Figure 9 are MCD-allowed: $\Psi_1 \rightarrow \Psi_2$ and $\Psi_1 \rightarrow \Psi_3$. These two transitions are predicted to be split by ~1600 cm^{-1} based on the energy splitting of the states (Figure 9 and Supporting Information, Figure S5).

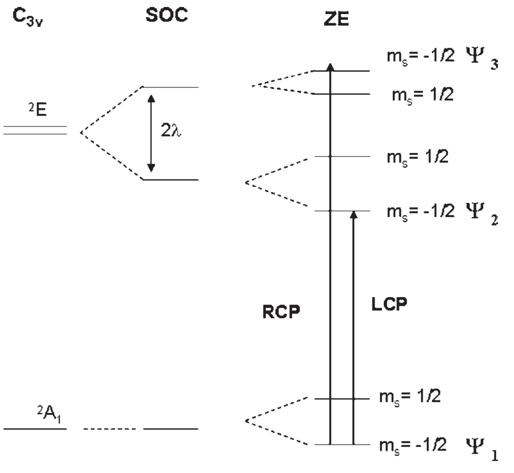

Figure 9. Energy diagram showing the effect of spin−orbit coupling (SOC) and the Zeeman effect (ZE) on the ground and excited states of Cu(II) and the prediction of a pseudo-A term.

The predicted sign of MCD transitions is determined by evaluating the effect of the right and left-circularly polarized electric dipole operators (m_+ and m_- respectively) between the initial and final state wave functions.[38] From this analysis, the $\Psi_1 \rightarrow \Psi_2$ transition is left-circularly polarized (positive MCD intensity) and the $\Psi_1 \rightarrow \Psi_3$ transition is right-circularly polarized (negative MCD intensity) (Figure 9 and Supporting Information). Thus the transitions from dxy/dx^2-y^2 to dz^2 would be observed as a pseudo-A term split by ~1600 cm^{-1} with the lower energy feature having positive MCD intensity. A parallel analysis was also performed for the transition from dxz/dyz to dz^2 and second pseudo-A is predicted with a smaller peak to peak splitting (~800 cm^{-1}) (Supporting Information, Figure S5). Both group theory predicted pseudo-A terms would have x,y-polarization ($^2A_1 \rightarrow {}^2E$ in C_{3v}).[38]

In the experimentally observed MCD spectrum of $[TMG_3trenCuO_2]^+$ (Figure 2B), Bands 1 and 2 are

---

(49) Note that the diagram in Figure 8 was constructed from DFT-calculations of the ground state of $[TMG_3trenCuO_2]^+$. In correlation to excited states, electronic relaxation will shift the charge transfer transitions to higher energy relative to the d to d transitions because of differences in electron repulsion, as is experimentally observed.

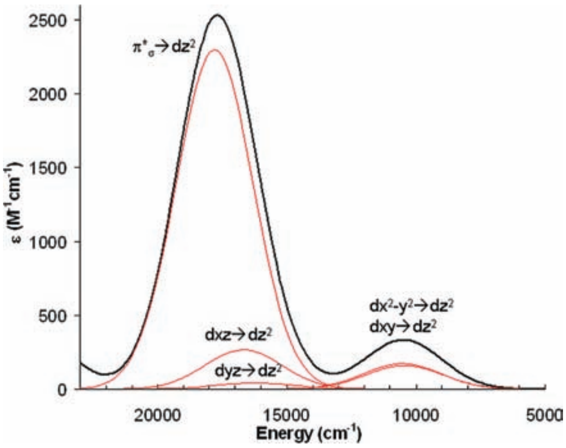

Figure 10. TD-DFT calculated absorption spectrum of $[TMG_3trenCuO_2]^+$ (black) and its decomposition into individual Gaussian components (red).

x,y-polarized and are observed as a pseudo-A term split by 1,570 cm^{-1}, with the lower energy feature (Band 1) having positive MCD intensity. This behavior is consistent with the predicted intensity pattern, peak to peak splitting, and polarization of the transition from dxy/dx^2-y^2 to dz^2 allowing definitive assignment.

Experimentally, the second x,y-polarized pseudo-A term predicted by group theory (corresponding to dxz/dyz to dz^2) is not observed. Peak 4 (Figure 2) is assigned as a d→d transition based on its C_0/D_0 ratio but is observed as a single peak with negative intensity and z-polarization. To gain insight into the assignment of this feature and the origin of its observed z-polarization, TD-DFT calculations were performed on $[TMG_3trenCuO_2]^+$ (Figure 10 and Table 4).

The TD-DFT calculated lowest energy d→d transitions are the dxy and dx^2-y^2 to dz^2. The two calculated transitions are x,y polarized, of comparable oscillator strength ($f_{osc} = 0.0026, 0.0028$), and are nearly isoenergetic (within ~100 cm^{-1} with no SOC) (Table 4). The calculated energies and polarizations of these transitions are in good agreement with those experimentally observed for Bands 1 and 2.

The TD-DFT calculated dyz and dxz to dz^2 transitions are ~6,000 cm^{-1} higher in energy, and split by 430 cm^{-1} (without including SOC). The $dyz \to dz^2$ transition has very low oscillator strength ($f_{osc} = 0.0008$) and is 73% z-polarized. The $dxz \to dz^2$ transition has high oscillator strength ($f_{osc} = 0.0042$) and is also calculated to be 97% z-polarized (Table 4). These transitions are calculated at energies consistent with the experimentally observed Band 4 (Figure 2) and like Band 4, these calculated transitions are z-polarized. Thus Band 4 is assigned as the dyz/dxz to dz^2 transition, with the $dxz \to dz^2$ component having a dominant contribution to the intensity of the transition. Thus from the TD-DFT, the dxz and dyz to dz^2 transitions are z-polarized, which is not consistent with the C_{3v} predicted x,y-polarization.

However, a Mulliken population analysis of $[TMG_3trenCuO_2]^+$ reveals that the dxz MO of $[TMG_3trenCuO_2]^+$ has 19% axial amine nitrogen character. Steric interactions of the terminal methyl groups of the TMG_3tren ligand with the end-on bound superoxo tilt the TMG_3tren ligand cage relative to the $Cu(O_2)$ core, and as a result, the axial amine nitrogen is tilted off the z-axis ($\angle N_{ax}CuO = 173°$). This distortion lowers the symmetry from C_{3v} to C_s and enables the pseudo-sigma overlap of the axial nitrogen lone pair with a lobe of the dxz orbital (Figure 11, bottom contour) which induces the z-polarization.

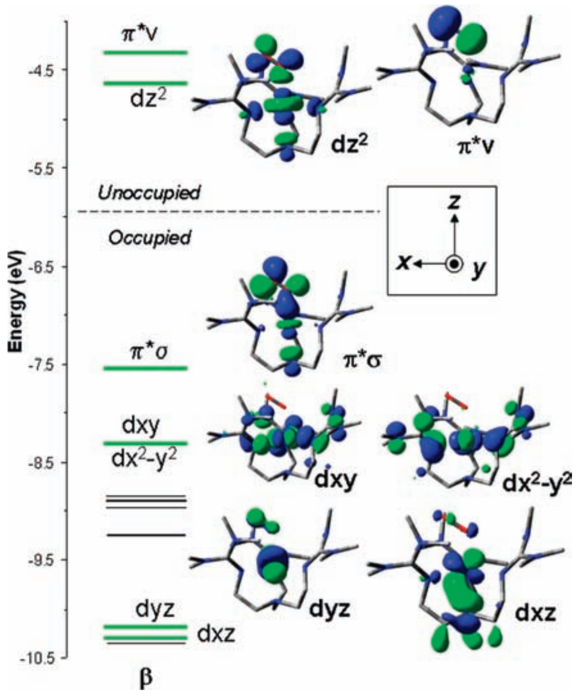

Figure 11. DFT-calculated spin down (β) MO diagram of $[TMG_3trenCuO_2]^+$.

The pseudo-A term observed for Bands 1 and 2 is not symmetric about zero, as expected for such a feature, and instead has increased net positive MCD intensity. The origin of this behavior is interstate SOC between this pseudo-A term and Band 4. The pseudo-A term (Bands 1 and 2) is x,y-polarized; and the negative Band 4 is z-polarized. The dxz donor orbital of Band 4 SOCs with the dx^2-y^2 and dxy donor orbitals of Bands 1 and 2 through the L_x, L_y operators which induces this interstate pseudo-A term behavior. The result of this interaction is an increased net positive intensity for the Band 1 and 2 pseudo-A term and negative intensity for Band 4 (Supporting Information, Figure S6). From the ratios of the observed peak areas, this interstate SOC accounts for ~40% of the intensity of Band 4 with the remainder originating from interstate SOC with other higher energy features.

3.6.2. Charge Transfer and Intraligand Transitions.

Band 5 (22,500 cm^{-1}) was assigned as a superoxo to copper charge transfer (LMCT) transition based on its low C_0/D_0 ratio and the significant enhancement of ν(Cu−O) and ν(O−O) within its absorption envelope (Sections 3.1 and 3.3). The TD-DFT calculated LMCT transition from the superoxo π^* in the $Cu-O_2$ x,z plane (π^*_σ) to the Cu dz^2 is in qualitative agreement with the observed Band 5 (Figure 10). The calculated LMCT is higher in energy than the d→d transitions (17,802 cm^{-1}), is intense, and is z-polarized, as experimentally observed for Band 5.

In addition to d→d and LMCT transitions, the TD-DFT calculations predict an intra-superoxo ligand (IL) transition corresponding to excitation of an electron

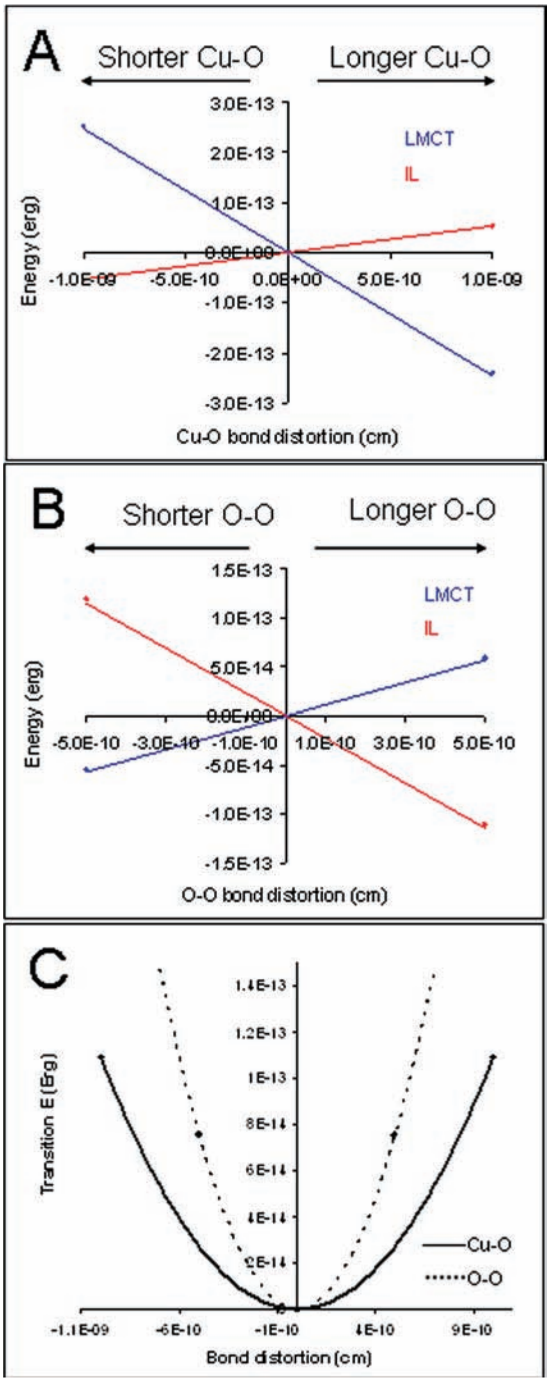

Figure 12. TD-DFT calculated LMCT (blue) and IL (red) transition energies as a function of distortion of the Cu–O (A) or O–O (B) bonds and the total ground state energy as a function of the Cu–O (solid line) and O–O (dotted line) bond distortions (C).

Table 5. Summary of TD-DFT Calculated Excited State Distortion Parameters

	Cu–O		O–O	
	LMCT	IL	LMCT	IL
$E_{\text{transition}}$/ displacement (Erg/cm)	-2.5×10^{-4}	5.4×10^{-5}	1.1×10^{-4}	-2.3×10^{-4}
$k_{\text{calc.}}$ (dyn/cm)	2.1×10^{5}		6.0×10^{5}	
Δr (calc.) (Å)	0.12	−0.025	−0.018	0.038
$\lvert\Delta r\rvert$ (exp.) (Å)	0.26	~0	0.06	0.10

between the two superoxo π^* orbitals in Figure 8, from the π^*_σ (x,z plane) to the π^*_v (x,y plane) at 7,199 cm^{-1}. Such a transition would not be expected to have significant MCD intensity as no perpendicularly polarized transition is capable of effective SOC with the IL transition. Experimentally, a superoxo IL transition has not been unambiguously assigned for any metal-superoxo complex. For $[\text{TMG}_3\text{trenCuO}_2]^+$, Band 3 has absorption intensity but has no significant MCD intensity consistent with an IL transition. However, the experimental energy of Band 3 (13,000 cm^{-1}) is considerably higher than the TD-DFT calculated π^*_σ to π^*_v transition energy of 7,199 cm^{-1}. Thus the experimental rR profile of $[\text{TMG}_3\text{trenCuO}_2]^+$ in Band 3 (Figure 6), where there is considerable enhancement of ν(O–O) but not ν(Cu–O), was used to evaluate this assignment.

TD-DFT calculations were used to predict the excited state distortions and thus expected resonance enhancements of the O–O and Cu–O stretches in a superoxo IL transition as compared to those in a LMCT transition. These computational distortions can then be compared to the experimental values obtained for Band 5 (LMCT) and Band 3 (Section 3.4). To computationally evaluate these distortions, each bond (Cu–O or O–O) was systematically varied, and the resulting change in energy of each TD-DFT calculated transition was determined (Figure 12 A and B). The computationally predicted distortion of the Cu–O and O–O bonds is given by the slope of the resulting linear curves (expressed in erg/cm) divided by the bond force constant (in dyn/cm). To computationally generate the Cu–O and O–O force constants, the total ground state energy of $[\text{TMG}_3\text{trenCuO}_2]^+$ was determined for a series of distortions along Cu–O and O–O, and each resulting curve was fit to a parabola (Figure 12C). The calculated Cu–O and O–O force constants are 2.1 mdyn/Å and 6.0 mdyn/Å, in reasonable agreement with the NCA calculated values (1.64 mdyn/Å and 5.76 mdyn/Å, respectively, Section 3.3). From this analysis, Δr(Cu–O) = 0.12 Å and Δr(O–O) = −0.018 Å for the LMCT transition and Δr(Cu–O) = −0.025 Å and Δr(O–O) = 0.038 Å for the IL transition (Table 5).

The experimentally observed excited state distortions qualitatively agree with those predicted from TD-DFT slopes (Table 5) and support the assignment of Band 3 as a superoxo IL transition. The LMCT transition (Band 5) excited state has a large Cu–O distortion (0.26 Å (exp.), 0.12 Å (calc.)) and relatively small O–O (0.06 Å (exp.), −0.018 Å (calc.)), while the IL transition (Band 3) excited state has twice the O–O distortion (0.10 Å (exp.), 0.038 Å (calc.)) and a much smaller Cu–O distortion (~0 Å (exp.), −0.025 Å (calc.)). Note that a parallel calculation has been done for the possibility of a MLCT transition. This predicts a Cu–O elongation and hence resonance enhancement in this vibration, which is not experimentally observed. This is consistent with the TD-DFT calculation of the MLCT at higher energy than the LMCT (Table 4) and supports the assignment of Band 3 as an IL transition. In summary, we have rigorously assigned the d→d transitions and superoxo to Cu(II) CT, and for the first time definitively observed a superoxo IL transition.

4. Discussion

In this study a combined spectroscopic and theoretical approach has been used to define the detailed electronic

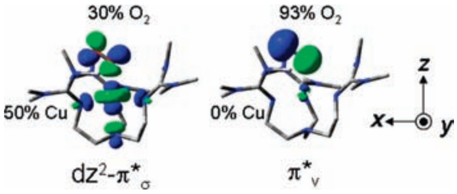

Figure 13. Two orthogonal magnetic orbitals of $[TMG_3trenCuO_2]^+$.

structure of the end-on bound copper-superoxo complex $[TMG_3trenCuO_2]^+$. Simultaneous fits of the low temperature absorption and MCD spectra of $[TMG_3trenCuO_2]^+$ resolved copper ligand field and charge transfer transitions and confirmed the ground state paramagnetism of the complex. The origin of this observed paramagnetism is the triplet ($S = 1$) ground state of $[TMG_3trenCuO_2]^+$, which is verified through VTVH-MCD studies. Ground state parameters and selection rules for transitions to excited states were determined from fits of these data. rR profiles of the Cu−O and O−O stretches of $[TMG_3trenCuO_2]^+$ led to the assignment of the dominant absorption feature of the complex as a superoxo π^*_σ to copper dz^2 (LMCT) transition and revealed the presence of an intra-superoxo π^*_σ to π^*_v (IL) transition at ~13,000 cm^{-1} (Band 3).

DFT and TD-DFT calculations on a model of $[TMG_3trenCuO_2]^+$ were found to accurately reproduce the experimentally observed geometry, ground state, spectroscopic features, and excited state geometries of the complex. The two singly occupied orbitals associated with the triplet ground state (the magnetic orbitals) are reflected in the two lowest lying unoccupied (virtual) β orbitals: the copper-based dz^2 and the superoxo-based π^*_v (perpendicular to the Cu−O$_2$ plane) (Figure 13). While the π^*_v orbital is purely superoxo-based (Figure 13, right), the spin density associated with the copper dz^2 orbital is partially delocalized into the superoxo in-plane π^*_σ orbital (Figure 13, left), and the superoxide based π^*_v is perpendicular to the Cu−O−O plane. These magnetic orbitals are orthogonal, which eliminates any antiferromagnetic coupling between the copper and the superoxide. The fact that the copper dz^2 orbital has significant π^*_σ character gives spin density from both magnetic orbitals on the oxygen atoms and thus leads to the ferromagnetically coupled ground state.

The copper-superoxo bonding of $[TMG_3trenCuO_2]^+$ is schematically represented in Figure 14. The energy separation of the π^*_v and dz^2 orbitals (Δ_3 in Figure 14) is a significant contributor to the ground state magnetism and is of considerable interest. For the triplet to be the ground state the energy separation of the π^*_v and dz^2 orbitals (Δ_3) must be smaller than the electron pairing energy (a sum of coulomb and exchange integrals) (Supporting Information, Figure S6). If Δ_3 became larger than the pairing energy, a singlet state would result from the transfer of the electron from the dz^2 to the π^*_v orbital. An upper limit of Δ_3 in $[TMG_3trenCuO_2]^+$ can be determined from the experimentally observed π^*_σ to π^*_v (IL) and superoxo π^*_σ to copper dz^2 (LMCT) transitions. This energy difference provides an upper limit for Δ_3 as the IL transition energy should decrease relative to Δ_2 and the LMCT transition energy should increase relative to Δ_1 because of differences in electron repulsion in the excited states (Supporting Information). Thus, $\Delta_3 < 9{,}500$ cm^{-1}.

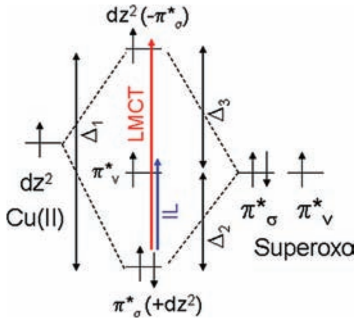

Figure 14. Schematic MO diagram of the copper-superoxo bonding in $[TMG_3trenCuO_2]^+$. The LMCT (red) and IL (blue) transitions are shown, as are the orbital energy separations (Δ_n). The π^*_σ (+dz^2) MO is dominantly superoxo-based and σ-bonding to dz^2 and the dz^2(-π^*_σ) MO is dominantly copper-based and σ-antibonding to π^*_σ.

To estimate the pairing energy, the energy of the excited state singlet (with two electrons in the π^*_v orbital) was computationally determined. The calculated difference between this excited state and the ground state is 7,970 cm^{-1}, and is equal to the pairing energy minus Δ_3. Δ_3 is less than the energy difference of the LMCT and IL transitions. TD-DFT calculations (employing the same calculation used to estimate the singlet energy) predict the energy of these two transitions (Table 4) and thus provide a computational estimate of Δ_3(calc.) $< 10{,}600$ cm^{-1}, which is in reasonable agreement with experiment. Combining these two results, an upper limit of the pairing energy for two electrons in the π^*_v in Figure 14 is ~18,600 cm^{-1}.

In summary, the electronic structure of the crystallographically characterized end-on bound superoxo-Cu(II) complex $[TMG_3trenCuO_2]^+$ has been defined through spectroscopic studies (absorption, MCD, VTVH-MCD, and rR excitation profiles) coupled with DFT calculations. The triplet ground state of $[TMG_3trenCuO_2]^+$ results from having two perpendicular magnetic orbitals, and, using the experimentally observed LMCT and IL transition energies, the energy splitting of these orbitals was found to be less than 9,500 cm^{-1} in $[TMG_3trenCuO_2]^+$ which is considerably less than the spin pairing energy for two electrons in π^*_v. The spectroscopically validated electronic structure calculations presented here provide new insight into the frontier orbitals involved in the reaction mechanism of the non-coupled binuclear Cu enzymes and will be the subject of further investigation.

Acknowledgment. This research was supported by NIH Grants DK31450 (E.I.S) and GM28962 (K.D.K). J.S.W is grateful for support from the William S. Johnson fellowship. F.N. gratefully acknowledges financial support by the Max-Planck society via a Max-Planck fellowship. Mr. Andreas Göbels is acknowledged for help with MCD measurements in the early stages of this project.

Supporting Information Available: MCD and rR spectra of $[TMG_3trenCuO_2]^+$, DFT results using the UBP86 and UBP38 functionals, interstate and intrastate SOC analysis, Coulomb and exchange integrals for LMCT and IL transitions, complete force field from NCA, Cartesian coordinates of the DFT-optimized geometry of $[TMG_3trenCuO_2]^+$, complete ref 30. This material is available free of charge via the Internet at http://pubs.acs.org.

---

(50) Yamaguchi, K.; Jensen, F.; Dorigo, A.; Houk, K. N. *Chem. Phys. Lett.* **1988**, *149*, 537–542.